A new analysis strategy for detection of faint γ-ray sources with Imaging Atmospheric Cherenkov Telescopes

Y. Becherini, A. Djannati-Ataï, V. Marandon, M. Punch, S. Pita

To cite this version:

Y. Becherini, A. Djannati-Ataï, V. Marandon, M. Punch, S. Pita. A new analysis strategy for detection of faint γ-ray sources with Imaging Atmospheric Cherenkov Telescopes. Astroparticle Physics, 2011, 34 (12), pp.858-870. ⟨10.1016/j.astropartphys.2011.03.005⟩. ⟨hal-00751218⟩

HAL Id: hal-00751218
https://hal.science/hal-00751218v1

Submitted on 13 Nov 2012

A new analysis strategy for detection of faint γ-ray sources with Imaging Atmospheric Cherenkov Telescopes

Y. Becherini, A. Djannati-Ataï, V. Marandon, M. Punch, S. Pita

PII: S0927-6505(11)00067-3
DOI: 10.1016/j.astropartphys.2011.03.005
Reference: ASTPHY 1587

To appear in: *Astroparticle Physics*

Received Date: 5 December 2010
Revised Date: 12 March 2011
Accepted Date: 18 March 2011

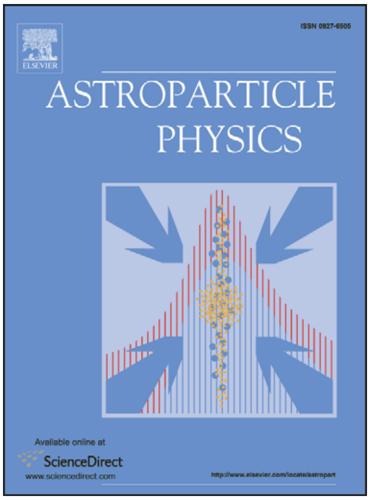

Please cite this article as: Y. Becherini, A. Djannati-Ataï, V. Marandon, M. Punch, S. Pita, A new analysis strategy for detection of faint γ-ray sources with Imaging Atmospheric Cherenkov Telescopes, *Astroparticle Physics* (2011), doi: 10.1016/j.astropartphys.2011.03.005

A new analysis strategy for detection of faint γ-ray sources with Imaging Atmospheric Cherenkov Telescopes

Y. Becherini*, A. Djannati-Ataï, V. Marandon, M. Punch, S. Pita

AstroParticule et Cosmologie (APC), 10, rue Alice Domon et Léonie Duquet, F-75205 Paris Cedex 13, France;
UMR 7164 (CNRS, Université Paris Diderot – Paris 7, CEA, Observatoire de Paris

---

Abstract

A new background rejection strategy for γ-ray astrophysics with stereoscopic Imaging Atmospheric Cherenkov Telescopes (IACT), based on Monte Carlo (MC) simulations and real background data from the H.E.S.S.[1] experiment, is described. The analysis is based on a multivariate combination of both previously-known and newly-derived discriminant variables using the physical shower properties, as well as its multiple images, for a total of eight variables. Two of these new variables are defined thanks to a new energy evaluation procedure, which is also presented here. The method allows an enhanced sensitivity with the current generation of ground-based Cherenkov telescopes to be achieved, and at the same time its main features of rapidity and flexibility allow an easy generalization to any type of IACT. The robustness against Night Sky Background (NSB) variations of this approach is tested with MC simulated events. The overall consistency of the analysis chain has been checked by comparison of the real γ-ray signal obtained from H.E.S.S. observations with MC simulations and through reconstruction of known source spectra. Finally, the performance has been evaluated by application to faint H.E.S.S. sources. The gain in sensitivity as compared to the best standard *Hillas* analysis ranges approximately from 1.2 to 1.8 depending on the source characteristics, which corresponds to an economy in observation time of a factor 1.4 to 3.2.

Keywords: γ/hadron discrimination; weak γ-ray sources; Imaging Atmospheric Cherenkov Telescopes; multivariate analysis; boosted decision trees.

---

1. Introduction

Very High Energy (VHE) γ-rays interact in the Earth's atmosphere, giving rise to highly relativistic showers which produce a few-nanosecond flash of Cherenkov photons in a "light pool" of ~ 250 m diameter. This can be detected by one or more ground-based telescopes, which collect this light using a mirror that reflects it onto a camera composed by an array of photomultipliers, converting the photons to a charge per pixel[2], and thus

---

*corresponding author: Yvonne.Becherini@apc.univ-paris7.fr, Tel: +33 1 57 27 61 58

[1] High Energy Stereoscopic System, see [1].

[2] For example, in the first phase of the H.E.S.S. experiment, the reflective mirror area is 107 m^2 and the pixel size is 0.16°, which is quite well adapted to the shower image size, with four such telescopes spaced by 120 m making up the stereoscopic array, see [3].

giving an image of the shower as seen by each telescope. γ-ray induced atmospheric showers have a rotational symmetry around the shower axis (neglecting geomagnetic effects), which results in elliptical images on the cameras. By combining the information from all the shower images seen, the arrival direction and the energy of the γ-ray can be reconstructed by well-established methods [2, 3]. The γ-ray signal is, however, drowned out by an enormous number of background air showers initiated by charged hadronic cosmic-rays. Contrarily to the γ-rays, the hadronic component of air showers is characterized by an asymmetric development of the particle cascade due to the hadronic interactions, which have large transverse momenta, and due to longer-lived muons reaching the telescope altitude.

After decades of research [5], great progress has been made in the field of VHE γ-ray astronomy in recent years, with the advent of the new generation of IACTs. The major keys to this success have been stereoscopy – offering a three-dimensional view of the atmospheric shower – and fast imaging cameras characterized both by their time response at the nanosecond scale and by a fine pixel granularity. These features have led to larger effective detection areas, a better angular resolution and a much improved discrimination power against the abundant cosmic-ray background. Nonetheless, the detection using standard analysis methods of sources at the level of 1% of the Crab nebula flux requires several tens of hours with arrays such as H.E.S.S. or VERITAS, even at their optimal sensitivity, out of ~ 1000 h/year of available good-weather moonless nights. This observation time needed for detection of very low-flux sources, for the discovery of new classes of γ-ray emitting sources, or for detailed morphological studies of extended sources can even become prohibitively long if mirror ageing occurs, causing an increase in threshold energy and thus a decrease in sensitivity.

Long experience has demonstrated the robustness against changing data-taking conditions of the standard Hillas-parameter based analysis (see [3] and also a short description in Sec. 2), essentially because of its stability under variable conditions, allowing its application to the entire set of IACTs world-wide since the 1980's. However, this kind of analysis does not exploit the correlation between images of the same shower as seen by different telescopes in a simple way, nor take advantage of fine-pixelization imaging. So, in recent years, additional methods have been developed in order to enhance the analysis sensitivity by fitting a model of the Cherenkov photons produced by a γ-ray shower to the images seen by each telescope, overcoming the above-mentioned limitations.

A first successful development was carried out over a decade ago for the CAT experiment in mono-telescope mode [6] with the 2D-model, where the image of the shower (in particular its longitudinal profile but also its transverse profile) is used to predict the angular origin of the event along the image axis, allowing the event direction on the sky to be obtained, as well as giving a χ^2-based discrimination variable for background rejection. This method has subsequently been improved (passing from a χ^2 minimisation to a maximum-likelihood, among other developments), and has been optimized to take full advantage of the stereoscopy provided by H.E.S.S. (see [7]). In addition, a three-dimensional (3D-model) reconstruction method has been introduced in H.E.S.S.

[4], where the result of the fit is a set of parameters describing the shower characteristics and where the selection analysis cuts are defined on the physical shower properties, rather than on the likelihood value. An upgraded version of the 3D-model analysis introduced a cut based on a χ^2 value in order to include the information from untriggered telescopes, see [8]. More recently, two different types of multivariate analyses (MVA) have been applied for H.E.S.S.: the first using Hillas-parameter based discriminant variables [9]; the second using discrimination based on Hillas-parameter based variables, plus 3D-model parameters and 2D-model goodness-of-fit [10].

The new method presented in this paper is based on an MVA approach optimized for the detection of low-flux sources, in which new ideas have also been implemented. First of all, the decision was taken to explore only discriminant parameters which are not a goodness-of-fit value, principally so as to lower the sensitivity of the analysis to uncertainties due to NSB variations. Indeed, in order for the systematics due to the NSB to be under control, goodness-of-fit based discrimination analyses need a rather precise knowledge of the underlying probability distribution (for likelihood fits)[3] of the pixel response to γ-ray showers and noise, together with its variation as a function of the NSB rate (see for example Sec. 3.7 of [7] and the χ^2 definition of [6]). These distributions may also be sensitive to imperfections of the electronics or the acquisition system and their drift over time, which might be difficult to reproduce[4] or time-costly to implement with MC simulations of the instrument. Avoiding such types of parameters should provide a more “portable” method, applicable to many current and future IACTs. Secondly, the information carried by the 3D-model about the predicted shape of γ-ray images on the cameras is found to provide additional discrimination power when the Hillas moments of the predicted images are calculated and used to derive new discriminant variables. Thirdly, an energy reconstruction method has been developed explicitly for this work, the conception of which has allowed the definition of two new discriminant parameters. These parameters, combined with a third new one – all of which are detailed below – provide additional power for hadron rejection. Special attention has been paid in this work to the cut optimization for different expected source characteristics (intensity and spectral hardness), as well as for studies of source morphology.

After a brief overview of the choices made for stereo reconstruction (Sec. 2) a versatile γ-ray energy reconstruction algorithm will be presented in Sec. 3, which is used as the basis for two newly-developed parameters. The parameters chosen for the γ/hadron discrimination are introduced in Sec. 4, while the details of the multivariate event classification method are presented in Sec. 5. The stability of the method is tested through comparison of MC simulations and real γ-ray data in Sec. 6. Finally, in Sec. 7 the performance is evaluated through application to H.E.S.S. sources.

---

[3] Or its error in case of a χ^2 fit.

[4] Some years of operation experience have been found to be necessary to understand and characterize such effects.

2. Stereo reconstruction

The steps of the shower reconstruction process used for the present work are described here. First of all, the images triggered by the event in the telescopes are cleaned so as to eliminate the pixels not containing a significant fraction of the Cherenkov photon signal (comparable to the NSB fluctuations) using the methodology described in [3][5]. The charges of the selected pixels are used to calculate the first and second moments of the images in each telescope, allowing the "Hillas parameters" to be derived (equivalent to fitting an ellipse to each image). A Hillas ellipse is characterized by its *length* and *width*, as well as by its position with respect to the camera centre, by the total charge in photo-electrons (p.e.), and by its main axis direction. Images whose centres-of-gravity fall near the edge of the cameras are discarded so as to minimize shower parameter misreconstruction due to image truncation; all the remaining images passing a pre-defined charge threshold are used to calculate the shower arrival direction and the intersection of the shower axis with the ground (also known as *impact position*), see [2, 3]. The geometry of the stereoscopic images allows the slant depth of the shower maximum to be estimated, assuming the centre of gravity of the images to be the projection of the maximum into the image plane.

The shower characteristics derived from the Hillas-parameter based variables are useful as such, but also as the first guess for the subsequent 3D-model optimization [4]. In the 3D-model, the γ-ray shower is modelled by a 3D-photosphere of Cherenkov photon origins in the atmosphere which is assumed to have a Gaussian distribution along all axes. This photosphere is described by eight parameters which are intrinsic to the shower: the direction and the impact position of the incident γ-ray, the photosphere length (along the shower axis) and transverse width (rotational symmetry around the shower axis being assumed), the slant depth of the shower maximum, and the number of Cherenkov photons generated by the electrons and positrons in the shower development. The 3D-model is used to predict the distribution of Cherenkov light in the cameras of a telescope array; then the intrinsic parameters of the shower are adjusted to achieve a good fit (using a maximum-likelihood optimization) of the ensemble of γ-ray shower images.

Given the Hillas and the 3D-model reconstruction procedures, two estimations of the event direction are available. The 3D-model point-spread-function (PSF) is better than that provided by the Hillas-parameter based reconstruction for energies below 500 GeV, whereas the inverse applies for higher energies. In this work, the Hillas-parameter based direction has been chosen for simplicity of implementation. Studies of the use of optimized combination of the two reconstructed directions will be undertaken for a future upgrade.

---

[5] The two-threshold image cleaning used in this work is of type 5–10 p.e.; and a pixel is also rejected if its charge is less than 3σ above its pedestal level. This is the case for the standard H.E.S.S. analysis. Other IACTs use thresholds which are adapted to their instruments.

3. Energy reconstruction

In ground-based γ-ray astronomy, sources are observed under various conditions of zenith angle, under which the images produced by γ-ray showers propagating in the atmosphere vary markedly, and the shower images also vary depending on the impact parameter of the shower with respect to the given telescope position (see for example the two-dimensional image profiles for such varying conditions in [11]). In addition, sources may be observed at different offsets with respect to the centre of the camera, resulting in different detector responses. Moreover, any loss of photon collection or detection efficiency can play an important role in the evaluation of the total image charge amplitude. Therefore, the data analysis in this field is characterised by a wide use of lookup tables, in which the γ-ray image characteristics as a function of the varying data taking conditions are stored to allow the modelling of the detector response to signal events.

The energy of the γ-ray shower can be reconstructed by using such lookup tables generated either with the Hillas-parameter based information, or with that provided by the 3D-model. However, the method for the evaluation of the energy with the 3D-model requires the convergence of the model fit, which is not guaranteed, especially for low-charge two-telescope events. As a generic method usable for all analysis configurations was deemed preferable, the choice was made to work in the Hillas-parameter based reconstruction framework. The proposed method of calculating the γ-ray energy has the advantage of being flexible, because the definition of the charge profiles can be performed with any kind of γ-ray simulation, and moreover, the energy evaluation phase is relatively fast with respect to other alternative methods, such as those requiring minimization [12]. The energy reconstruction method presented here is composed of two separate phases: a preparatory phase and an evaluation phase.

3.1. Preparatory phase

The preparatory phase requires the generation of lookup tables (*charge profiles*, see for example Fig. 1a) of the sum of the charges measured in a simulated γ-ray cleaned image as a function of the impact parameter (referred to below as R). These are created for discrete sets of values of the simulated energy E_{true}, of zenith angles Θ, of values of the mirror efficiency M, of offsets D of the shower angular origin with respect to the centre of the camera, and for multiple bands of reconstructed shower maximum depths H (as estimated from the Hillas parameters of the images). Note that these charge profiles are related to the Cherenkov light profile on the ground, but as detected in the images seen by the telescopes (including the photomultiplier efficiency with wavelength and image cleaning effects, etc.).

3.2. Energy evaluation phase

The energy evaluation phase consists of the use of these pre-generated charge profiles to calculate the event energy based on a weighted combination of the estimates of the energy in each telescope. The strategy for the evaluation of the energy in each telescope can be easily visualized by a tree, see Fig. 1b. For an event having a triggered telescope

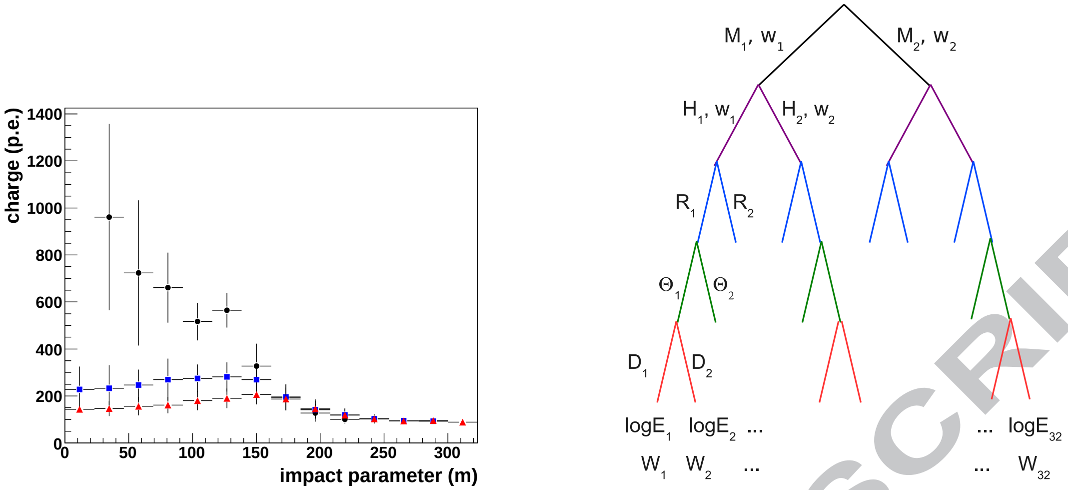

(a)

(b)

Figure 1: (a) Profiles of the charges of the cleaned images in the cameras as a function of the reconstructed impact parameters at three different observing angles 0° (points), 32° (squares) and 41° (triangles), for a given energy, shower maximum, offset and mirror efficiency; the error bars shown represent the spread of the distributions. (b) Schematic of the tree used for the evaluation of the event energy for each telescope. For an event having a zenith angle $\Theta_{\rm reco} \in [\Theta_1, \Theta_2]$, an offset $D_{\rm reco} \in [D_1, D_2]$, a maximum depth $H_{\rm reco} \in [H_1, H_2]$, an impact parameter $R_{\rm reco} \in [R_1, R_2]$, and being observed in a telescope having a mean mirror efficiency $M_{{\rm Tel}_i} \in [M_1, M_2]$, the $\log_{10} E_j$ and the weight W_j are calculated for each branch of the tree and then the different values are combined to evaluate the event energy per telescope $E_{{\rm Tel}_i}$.

Tel$_i$ with an associated mirror efficiency $M_{{\rm Tel}_i}$ and a measured charge $q_{{\rm Tel}_i}$, there are four reconstructed parameters: the zenith angle $\Theta_{\rm reco}$, the offset $D_{\rm reco}$, the maximum depth $H_{\rm reco}$ and the impact parameter with respect to the position of the telescope $R_{\rm reco}$. The weight of each branch of the tree W_j can be calculated, where W_j is given by:

$$W_j = \prod_{k=1}^{5} p_k \quad \text{where} \quad p_k = w_k \quad \text{or} \; p_k = (1 - w_k) \; \text{depending on the branch taken,} \qquad (1)$$

and where the weights w_k are given by the interpolation of the nearest simulated values. As an example, for an event having a reconstructed zenith angle $\Theta_{\rm reco}$ the algorithm searches for the two fixed values $[\Theta_1, \Theta_2]$ between which to interpolate such that $\Theta_{\rm reco} \in [\Theta_1, \Theta_2]$, and applies a weight of $w_\Theta = (\Theta_{\rm reco} - \Theta_1)/(\Theta_2 - \Theta_1)$. For each branch of the tree, given the value of the measured charge $q_{{\rm Tel}_i}$, the event energy associated with the telescope can be retrieved using the charge profiles mentioned in Sec. 3.1, which were defined for a set of energy values. The energy in each triggered telescope can thus be easily calculated by a weighted mean on all the energy values and weights obtained from the $2^5 = 32$ branches:

$$\log_{10} E_{{\rm Tel}_i} = \frac{\sum_{j=1}^{32} [W_j \cdot \log_{10} E_j]}{\sum_{j=1}^{32} W_j} \qquad (2)$$

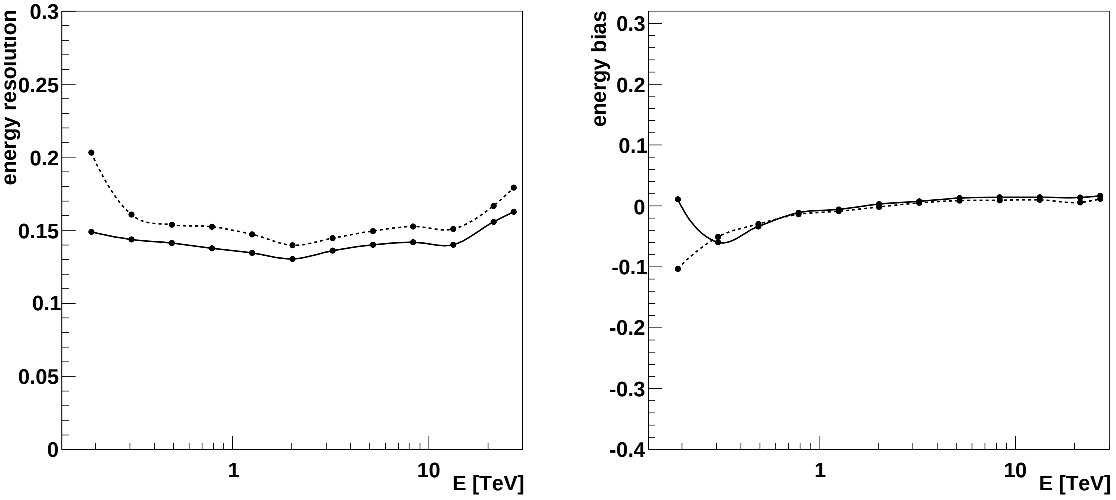

(a) (b)

Figure 2: Given the distribution of $\log(E_{\text{reco}}/E_{\text{true}})$, where E_{reco} and E_{true} are the reconstructed and simulated energy values, its standard deviation defines the energy resolution (a), and the mean value defines the bias (b). The two curves refer to two analysis configurations (40 p.e. and 150 p.e., dashed and continuous line respectively, see Sec. 5.4).

The energies E_{Tel_i} calculated separately for each triggered telescope are combined in the final step with a charge-weighted mean:

$$E_{\text{reco}} = \frac{1}{Q_{\text{tot}}} \sum_{i=1}^{N_{\text{Tels}}} \left[q_{\text{Tel}_i} \cdot E_{\text{Tel}_i} \right], \text{ where } Q_{\text{tot}} = \sum_{i=1}^{N_{\text{Tels}}} q_{\text{Tel}_i} \tag{3}$$

Q_{tot} being the total charge of the event. The resolution and bias of the current implementation of the algorithm can be seen in Fig. 2: in the energy range 0.2-30 TeV the resolution is almost stable at $\sim 15\%$, while the bias is better than 5% for $E > 0.3$ TeV.

4. Selected γ/hadron discriminant parameters

The definitions of the discriminant parameters take advantage of the information carried by the two different stereo reconstruction algorithms discussed in Sec. 2 (the 3D-model and Hillas-parameter based ones) and of the energy reconstruction algorithm introduced in Sec. 3.2. As will be mentioned in Sec. 5.3, the parameters have been chosen according to their discriminant power and in order to avoid strongly-correlated variables.

4.1. Hillas-parameter based discriminant variables

For a given reconstructed shower, two powerful discriminant parameters commonly used for stereoscopic arrays can be defined: a *Mean Scaled Length* (MSCL) and a *Mean Scaled Width* (MSCW). As described in [3], lookup tables are prepared based

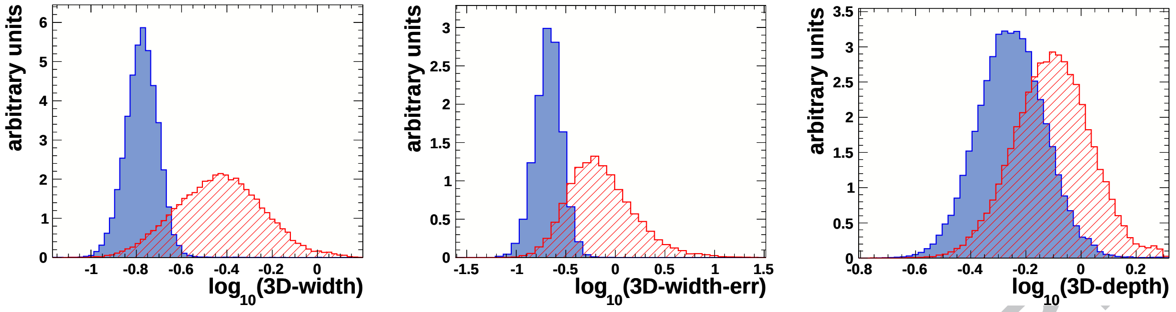

(a) (b) (c)

Figure 3: 3D-width (a) and 3D-width-err (b) for the H.E.S.S. array and for energies in the range 1–2 TeV. The 3D-depth (c) is shown for the range 100–300 GeV. All three parameters are shown for the 10–20° zenith angle range. Filled and hatched distributions represent the γ-ray simulated events and the measured cosmic-ray background, respectively.

on simulations, which contain the mean width and length and their respective rms scatter for a γ-ray as a function of the amplitude of the shower image in the camera and the impact parameter relative to the telescope. The MSCL and MSCW are then calculated as the mean values of the deviations of the measured lengths and widths from the predicted mean values, divided by their rms. In short, these mean scaled parameters indicate deviations of the shape of the detected images compared to those resulting from the γ-ray simulations, and hence allow for discrimination, see Fig. 7 of [3] for further details. The Hillas-parameter based reconstruction and discrimination have been the basis of a large number of discoveries in recent years, showing that these two simple scaled parameters were sufficient for an efficient γ/hadron discrimination in case of bright sources (i.e., $> 10\%$ C.U.[6]).

4.2. 3D-model based discriminant parameters

As described in Sec. 2, eight parameters are adjusted by the 3D-model fit, which also provides the error estimates for these parameters. Among these, two parameters, the *reduced 3D-width*[7] and the depth of shower maximum (*3D-depth*), together with the error on the former parameter (*3D-width-err*), have been retained for their high discriminant power. The distribution for the 3D-width for γ-rays (Fig. 3a) is narrower and has a peak at lower values compared to that of the background. The same applies to the 3D-width-err (Fig. 3b), showing that the model is not suitable for the representation of a hadron-induced shower, thus giving larger error values as a consequence, with an associated discrimination power. Moreover, it was found that the two 3D-width related

---

[6] "Crab Units", i.e., compared to a hypothetical source with the Crab nebula intensity and spectrum at the zenith angle of observation.

[7] As the Cherenkov photosphere is found to be dependent on the variation of the Cherenkov threshold with the altitude of the shower maximum, an efficient and dimensionless γ/hadron discrimination parameter called *reduced 3D-width* has been defined, though for simplicity this is referred to as the 3D-width in the following.

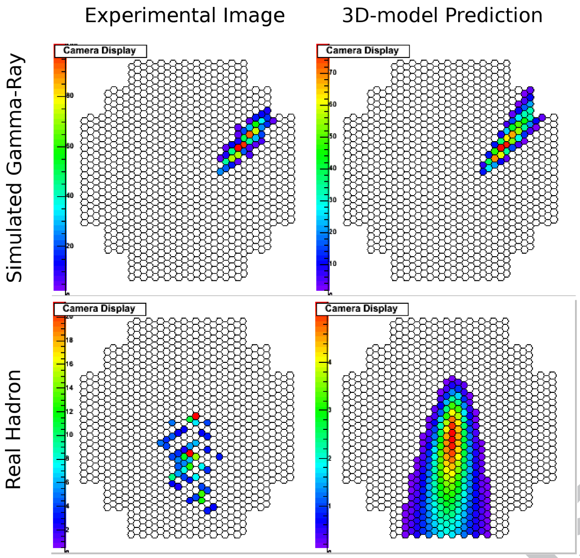

Figure 4: γ-ray and hadron images seen in a camera. The upper panels show the simulated γ-ray cleaned image (*left panel*) and corresponding prediction given by the 3D-model minimization (*right panel*), while the lower panels show a real cleaned hadron image and its corresponding 3D-model prediction.

parameters show a significant separation performance over the entire energy range, while 3D-depth (Fig. 3c) is highly discriminant for lower energies, with decreasing separation power with increasing energy, as will be shown also in Sec. 5.3.

4.3. New discriminant parameters

Beyond the five above-mentioned discriminant parameters, three new ones have been defined for the purpose of further enhancing the γ/hadron separation performance. Due to the difference in the shower development, especially regarding its rotational asymmetry/symmetry around the shower axis, even in the case where the fit of a hadronic shower with a γ-ray model (as for instance in [4]) succeeds, it may lead to incoherencies – in both shape and total charge – between the predicted shower images and those observed (or absent) in the individual telescopes (see Fig. 4). The alternative method proposed here is to explore these differences by defining additional Hillas parameters (here called *HillasOnModel* parameters) using the predicted images in the cameras, to which the same cleaning and moment calculation procedures are applied and which can be used to define new discriminant variables. In this way the inter-telescope correlations which are inherently included by the 3D-model optimization are further exploited in a simple Hillas-parameter based discrimination framework.

4.3.1. The Ω parameter

The discriminant parameter named Ω is based on the expected difference in the angular distance on the sky between the two reconstructed shower directions when using *Hillas* and the *HillasOnModel* ellipses:

$$\Omega = \log_{10}(\arccos(\hat{v}_{\mathrm{Hillas}} \cdot \hat{v}_{\mathrm{HillasOnModel}})) \tag{4}$$

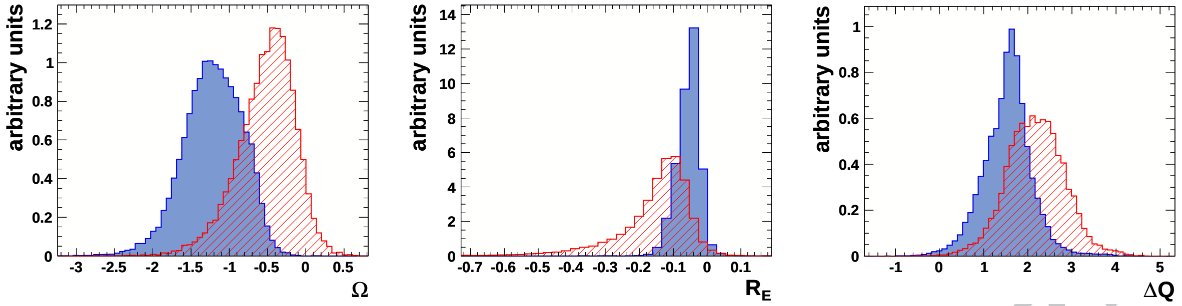

(a) (b) (c)

Figure 5: The Ω (a), R_E (b) and ΔQ (c) distributions for the energy range 1–2 TeV and for the zenith angle range 10–20°. The filled distributions correspond to the γ-ray events, while the hatched distributions correspond to the cosmic-ray background.

where $\hat{v}_{\text{Hillas}}$ and $\hat{v}_{\text{HillasOnModel}}$ are the normalized vectors corresponding to the two directions. The shift in the mean value of the Ω distributions (see Fig. 5a) is due to the fact that the difference in the major axis of the two ellipses is small for a well-fitted γ-ray and larger for a badly-fitted hadron.

4.3.2. The R_E parameter

The energy reconstruction procedure described in Sec. 3 allows the derivation of the following parameter based on the ratio of two reconstructed energy values:

$$R_E = \log_{10}\left[\frac{E_{\text{Hillas}}}{E_{\text{HillasOnModel}}}\right] \tag{5}$$

where the energy of the event, E_{Hillas}, is estimated with the Hillas parameters of the detected images, and the additional energy estimation, $E_{\text{HillasOnModel}}$, is carried out based on the *HillasOnModel* parameters. This ratio is expected to have small deviations from zero for well-reconstructed γ-rays, while for misreconstructed hadrons larger deviations are expected. The distributions of R_E for simulated γ-rays and for real background are illustrated in Fig. 5b, and these differ as expected, the background having a large tail towards smaller R_E.

4.3.3. The ΔQ parameter

The third new parameter also takes advantage of the new energy reconstruction procedure. Having calculated the event energy and knowing the reconstructed impact parameter of the event, the second phase of the procedure for the energy evaluation per telescope described in Sec. 3 can be inverted to find the expected image charges $\tilde{q}_{\text{Tel}_i}$ on each telescope. A discriminant parameter based on the deviation of $\tilde{q}_{\text{Tel}_i}$ with respect to the measured charges q_{Tel_i} can be defined using a least squares in charge:

$$\Delta Q = \frac{1}{Q_{\text{tot}}}\sum_{i=1}^{N_{\text{Tels}}}\left[\tilde{q}_{\text{Tel}_i} - q_{\text{Tel}_i}\right]^2 \tag{6}$$

where N_{Tels} is the number of telescopes in the array and Q_{tot} is the summed charge in all telescopes as defined previously in Eq. 3. For poorly-reconstructed events, an inconsistency between the energy evaluation and the reconstructed impact position is expected. Hence, the predicted charge $\tilde{q}_{\mathrm{Tel}_i}$ on a telescope for such an event is expected to be very different from the q_{Tel_i} measured (or not measured, in the case where a telescope did not trigger). As shown in Fig. 5c, the shape of the ΔQ distributions reflect the expected behaviour, the background events having larger values.

5. Multivariate analysis

In order to achieve an efficient hadron rejection, all the above-mentioned parameters are used within a multivariate discrimination scheme based on the TMVA [13] package within the ROOT [14] framework. Among all the available discrimination algorithms, this work had initially focused on neural networks (*Multi Layer Perceptron* or MLP) and on *Boosted Decision Trees* (BDT). During these early tests, it became immediately clear that the BDT technique was more stable and gave better results in terms of signal-to-background discrimination, thus confirming that this technique is the best out-of-the-box multivariate procedure, requiring minor adjustments to be applicable.

A summary of the operation of the BDT technique is given in App. A, with details particularly concerning the design of the decision trees, the difficulties which can be encountered through overtraining, and the best pruning strategies to apply for the case of IACTs. The multivariate classification technique consists of four main phases: the first one is the *training* (see App. A.1, A.2) where the “forests” of decision trees are constructed, with a set of events randomly chosen from the input. Then, in a second phase, the classifier performance is *tested* with an independent set of events, and *evaluated* (see App. A.3, A.4). This study led to a specific design of the decision trees, differing somewhat from the default options of the BDT procedure as implemented in TMVA. Since these details could be useful for the implementation of this technique for other IACTs, they are included in App. A.5. After the definition of the final cut values, the classifier is finally *applied* to the data (see App. A.6).

5.1. Simulated γ-ray and measured hadron background data samples

The γ-ray shower samples were produced by MC simulations with KASKADE[8] [15, 16, 17]. The γ-ray showers are simulated between 30 GeV and 120 TeV for two different azimuths (*North* and *South*), several zenith angle bands spaced regularly in $\cos(\theta_{\mathrm{zen}})$ (in steps of 0.05) from 0° to 70°, and for a point-like source. The resulting Cherenkov light is then propagated through the H.E.S.S. detector with SMASH[9][16], where the source position can be shifted to different offsets D from the centre of the camera (six D values spaced by 0.5° from 0° to 2.5° are simulated, where 2.5° corresponds to the radius of the H.E.S.S. field-of-view or FoV). Taking advantage of the large set of available H.E.S.S. data as a background sample, the use of time-consuming and marginally-reliable hadron

---

[8] One of the two shower simulation packages used in H.E.S.S., the other being Corsika[18].

[9] This program is one of the two available H.E.S.S. detector-response simulation programs.

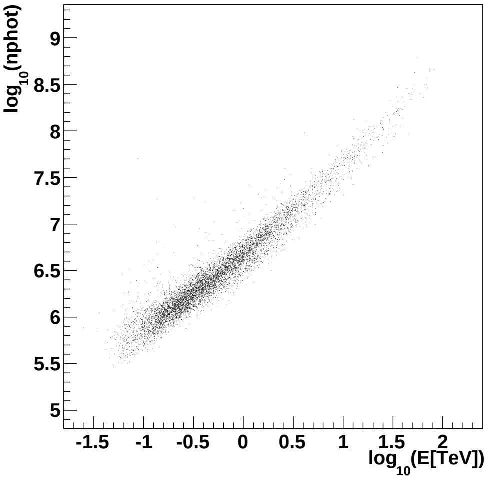

Bin	Interval in log$_{10}$(nphot)	Interval in E (TeV)
1	0.01 – 5.80	0.0 – 0.1
2	5.80 – 6.18	0.1 – 0.3
3	6.18 – 6.35	0.3 – 0.5
4	6.35 – 6.59	0.5 – 1.0
5	6.59 – 6.82	1.0 – 2.0
6	6.82 – 7.13	2.0 – 5.0
7	7.13 – 10.0	5.0 – 1000

Figure 6: *Left panel:* number of fitted photons in the reconstructed shower (*nphot*) as a function of the reconstructed energy in TeV (log scales). *Right panel:* the definition of the *nphot* bins and the approximate corresponding values (based on the left-hand figure) of the reconstructed energy (in TeV) are illustrated.

simulations could be avoided. The background was therefore extracted from extragalactic observations using regions of the camera which do not contain any known γ-ray source, at various zenith angles, and taking into account the northern or southern azimuth of the observations (to account for different geomagnetic field effects). All the hadrons reconstructed out to angles including the H.E.S.S. FoV plus 0.2° are taken into account.

5.2. Training and Test Configurations

A set of bins in energy, zenith angle, and telescope multiplicity (i.e., the number of triggering telescopes; two to four in the case of H.E.S.S.) are defined for the training/test phases of each of the implemented analysis configurations (see Sec. 5.4).

There are eight zenith angle bins and seven energy bins, in order to regroup the different classes of events showing similar properties. The shape of the parameter distributions for each defined group may differ from the other groups, leading to a different background rejection performance. The zenith angle bins are defined in 10° intervals from 0° up to 40°, then in 5° intervals, and finally in a single interval[10] from 55° to 90° for each of which seven energy bins are defined by the number of photons in the shower as fitted by the 3D-model (referred as to *nphot*), as shown in Fig. 6. The latter choice has been found to be effective in avoiding brusque variations in the final effective area.

The phase space is additionally subdivided in two bins in telescope multiplicity: one

---

[10] Note that the definition of zenith angle bins which are regularly spaced as a function of $\cos(\theta_{\mathrm{zen}})$ as used in the MC simulations is more convenient; however, the different choice used here for the MVA training has been imposed by some initial compatibility constraints with other modules inside the H.E.S.S. Analysis Package.

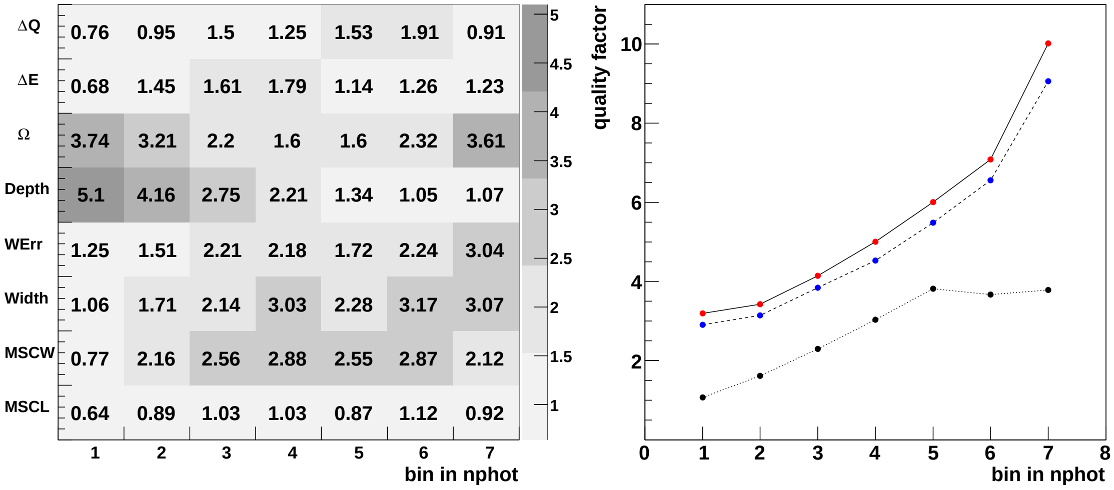

(a) (b)

Figure 7: (a) Two-dimensional plot of the importance of the parameters during training as a function of the bin in *nphot*. The value shown in each box is the sum over all zenith angle bins of the relative weights, given by the BDT training to each discriminant parameter (see text). *Depth*, *ErrW* and *RedW* refer to the 3D-depth, the 3D-width-err and the 3D-width, respectively (b) Quality factor (QF) as a function of the *nphot* bin for given γ-ray efficiencies, at a zenith angle of 0° and for a configuration having a charge threshold of 80 p.e. per telescope. Dotted, dashed and continuous lines represent the QF obtained with the following configurations of parameters: a first group (MSCL, MSCW), a second group (adding three 3D-model parameters), and a third group (adding the three new newly defined parameters), respectively.

for the two-telescope events and one for the three and four-telescope events, leading to a total of 112 bins altogether. This split has been motivated by the fact that for events which trigger only two telescopes, less information is available for geometric reconstruction, therefore leading to a parameter space which is considerably different with respect to that for events triggering three and four-telescopes. It should be noted that in order to avoid badly-reconstructed γ-ray events polluting the training and test phases, such events are excluded using a cut on the angular distance on the sky between the reconstructed event direction with respect to the source direction ($< 0.11°$).

5.3. Relative importance of the parameters for discrimination

The multivariate method *ranks* the discriminant parameters according to the frequency with which they are used in the splitting of the decision tree nodes. The values shown in the boxes of Fig. 7a are given by the sum of the relative weights given by the BDT training. It can be observed that at low energies ($E < 500$ GeV) the most important discriminant parameter is the 3D-model estimated depth of the shower maximum, with its importance decreasing as a function of energy. The second parameter in order of importance is Ω: while its discrimination performance is clearly high in all energy

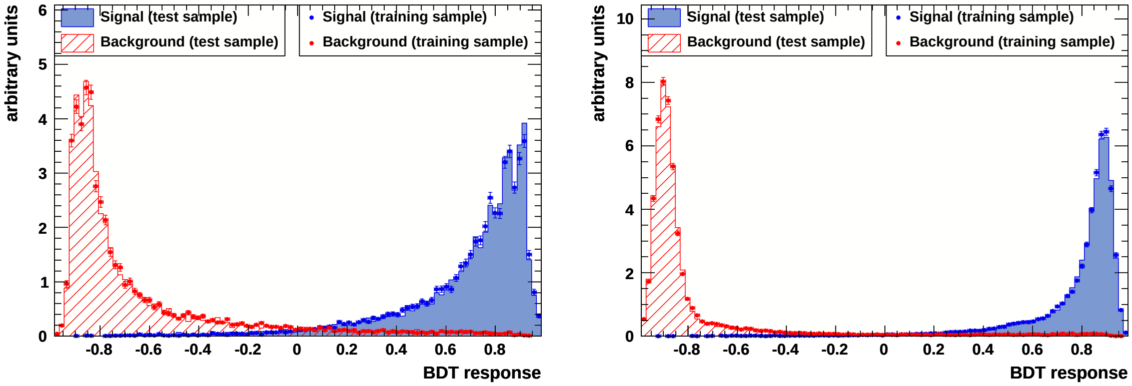

(a) (b)

Figure 8: The BDT classifier response to the BDT training and test phases for the bin between 10–20° in zenith, and between 1–2 TeV for two-telescope events (a) and for three-telescope and four-telescope events (b). The response to both the training and test samples are shown (points ans histograms respectively).

bins, it is more powerful at low energies[11] ($E < 500$ GeV, bin in $nphot \leq 3$) or high energies ($E > 5$ TeV, bin in $nphot \geq 7$). The least discriminant parameter in almost all cases is MSCL. The importance of the chosen parameters can also be evaluated by checking the relative quality factor when progressively adding groups of variables to the training, where the quality factor is defined as

$$Q = \frac{\epsilon_\gamma}{\sqrt{\epsilon_{\rm bkg}}}, \text{ where } \epsilon_{\gamma,\rm bkg} = N_{\rm cut}/N_{\rm reco} \tag{7}$$

with $N_{\rm cut}$, $N_{\rm reco}$ being the number of events after and before cuts, respectively, in a given bin. Three different test configurations are defined: the first group includes only MSCL and MSCW; the second comprises MSCL, MSCW plus the group of the three chosen 3D-model parameters; and the third adds the three new ones defined for the purpose of this work to the preceding groups. The results are given in Fig. 7b: a significant gain in performance is achieved when adding the group of the three 3D-model parameters to the Hillas-parameter based ones; and with the addition of the new parameter group a further $\sim 20\%$ of background is cut away, leading to an additional gain in Q of $\sim 12\%$.

Finally, it should be noted that investigation of the effects of the correlations between the discriminant parameters resulted in the elimination of a few parameters which had been defined at an early stage of the analysis development (see [20]). Optimization tests within the specific framework used here showed that the inclusion of pairs of highly-correlated variables resulted in a loss of discrimination performance, probably due to the overall development of the trees in the forest being more sensitive to fluctuations[12].

---

[11] Though Ω is still less discriminant than the depth at shower maximum.

[12] Tests of the TMVA functionality which implements parameter decorrelation provided inconclusive results, though this may be explored in further developments.

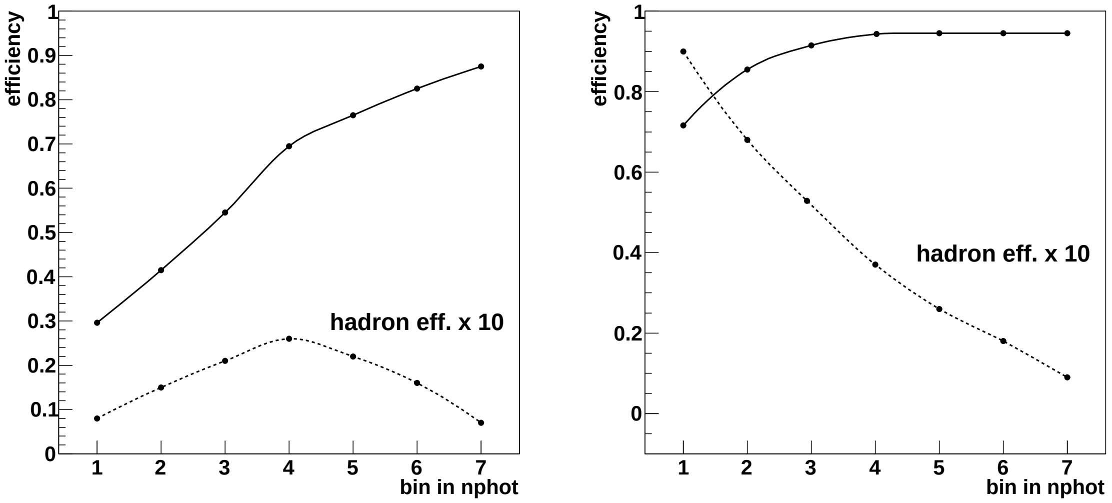

(a) (b)

Figure 9: Discrimination performance for the analysis configuration having a 110 p.e. charge threshold. The solid lines show the γ-ray efficiencies within the angular pre-cut mentioned in Par. 5.2, while the dashed lines show the corresponding hadron efficiencies multiplied by 10. These are shown as a function of the *nphot* bin for a zenith angle of 0°, (a) for two-telescope events and (b) for three and four-telescope events. The definition of the photon bins (*nphot*) can be found in Fig. 6.

5.4. Definition of cuts for different source types

The training on each event class described in Sec. 5.2 provides a separate BDT classifier (see Fig. 8 for two examples), on which the analysis cut is based. For the definition of the final cut values, the use of the highest significance criterion[13] provided by the BDT training process was found to be subject to statistical fluctuations. For this reason, γ-ray efficiency profiles as a function of energy were defined in order to optimize the detection sensitivity for sources with different fluxes, through an iterative optimization process. For illustration, the pre-defined γ-ray and corresponding background efficiencies for one analysis configuration, of the five described below, is shown in Fig. 9. For the purpose of the analysis of sources showing different spectral indices, five configurations are defined based on the following charge thresholds: 40, 60, 80, 110 and 150 p.e.

To achieve an optimal sensitivity for sources with spectral indices[14] $\Gamma \lesssim 3$ and fluxes above $\simeq 1\%$ C.U., an analysis configuration having a charge threshold of 80 p.e. (and a similar one at 60 p.e.) has been developed. This configuration is therefore adapted for most Galactic-plane observations, where most of the sources discovered have hard spectra (see [21]) and is also used for low-redshift extragalactic observations. For similar spectral indices but lower fluxes ($< 1\%$ C.U.), another configuration has been defined

---

[13] Which depends on the relative normalization between signal and background.

[14] Given a power-law photon differential flux in $E_{\mathrm{TeV}}^{-\Gamma}$.

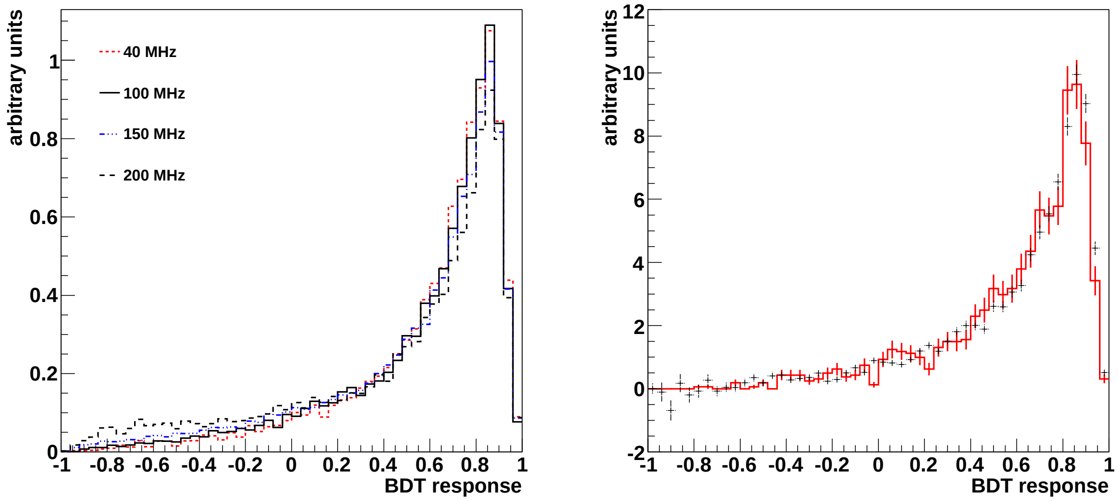

(a) (b)

Figure 10: (a) BDT response for simulated γ-rays for different NSB rates ranging from 40 to 200 MHz. The sample was simulated at Zenith and follows a power-law with differential index $\Gamma = 2$. The BDT response remains stable for NSB rates up to 150 MHz, the relative migration of events from the signal to the background range remaining well below 2%. For a larger rate of 200 MHz, the latter attains $\sim$10%, without significant impact on the measurements (see text). (b) BDT response for γ-ray simulated events (solid line) and real γ-ray events (crosses with error bars) from the Crab nebula.

with a charge threshold of 110 p.e. and for which the γ-ray efficiencies have been set so as to yield a lower rate of low-energy two-telescope events than the other configurations, see Fig. 9. These two characteristics help in reducing the lower energy fluctuations due to the background events, thus enhancing the sensitivity for this source class. For morphological studies of extended sources, a dedicated configuration has been developed which has an enhanced PSF, optimizing the performance in geometrical reconstruction by raising the charge threshold to 150 p.e.

For high-redshift extragalactic observations where the effect of γ-ray absorption becomes significant, steep-spectrum ($\Gamma \sim 3$) sources are naturally expected. To optimize the sensitivity for the detection of this class of sources, the image size threshold has been lowered to 40 p.e. in order to enhance the signal of the abundant lower energy events.

App. B discusses the instrument response functions associated with these configurations.

6. Robustness and consistency checks

6.1. Robustness with respect to variations of the NSB rate

One of the key points of the present approach is its ease of implementation without the need for calibration of the discriminant variables as a function of the NSB rate for a given FoV. With the H.E.S.S. telescopes, the NSB median value of the latter can vary

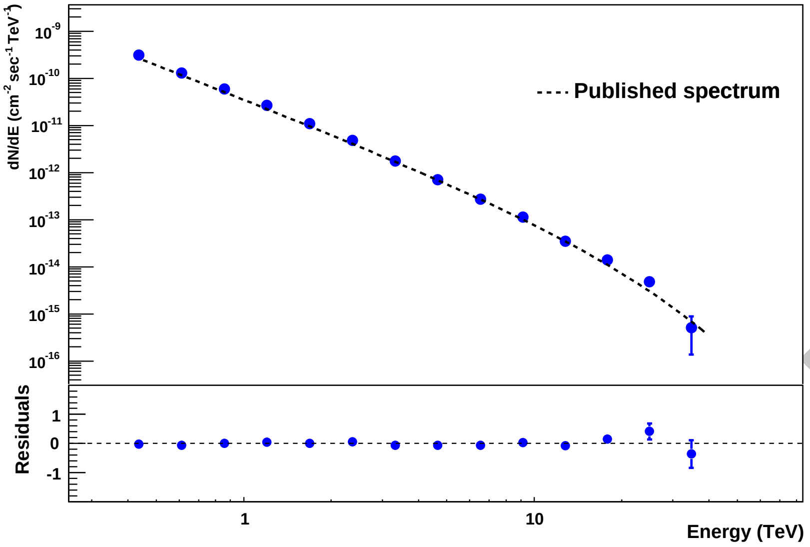

Figure 11: Reconstructed spectrum of the Crab nebula (points), showing an excellent agreement within the systematic errors with the published results (dashed line)[3]. The residuals are calculated with respect to the fitted spectral shape.

from few tens of MHz per pixel for extragalactic observations, up to ∼ 130 MHz for 95% of H.E.S.S. observations and for central parts of the Galactic plane. Fig. 10a shows the distribution of the BDT response for simulated γ-rays following a power-law ($\Gamma = 2$) at Zenith, with different NSB rates ranging from 40 to 200 MHz. The stability of the BDT response to NSB rates up to 150 MHz is remarkable: the relative migration of events from the signal to the background range remains well below 2%. For a larger NSB rate of 200 MHz, the migration attains ∼10%, however, the resulting systematic error on the effective area (i.e., 10%) remains dominated by the error due to the uncertainty in the energy scale [3], depending on the spectral index of the source. A check of the energy dependence of such an effect has also been carried out through reconstruction of simulated γ-rays following the same power-law and the same NSB levels as above. No significant bias was found on the measured spectral index. This was expected, since the choice of those variables already available (MSCL, MSCW, 3D-width, 3D-width-err, 3D-depth, see Sec. 4.1 and 4.2), and the definition of the new discriminant parameters (Ω, R_E and ΔQ, see section 4.3) was made following the study of their individual robustness with respect to the NSB rate.

6.2. Consistency checks using real γ-ray data

The consistency of the BDT response was checked by comparison of its distribution for simulated γ-rays to that of the signal from the Crab nebula. MC simulations were made for γ-rays with a spectrum following a power-law up to 100 TeV with a differential photon index $\Gamma = 2.6$, and a zenith angle of 46°, matching closely the chosen data-set.[15] As can be seen on Fig. 10b, there is a good agreement between the simulated sample's BDT distribution and that of the Crab nebula signal.

Finally, as is mandatory in VHE γ-ray astronomy, an overall consistency check of the analysis chain was performed by comparing the spectrum as measured with the present MVA approach to that obtained with the standard Hillas-parameter based one, for a source such as the Crab nebula [3]. As shown in Fig. 11, fitting an exponentially cut-off power-law to the data in the range 380 GeV to 44 TeV yields a flux of $I_0 = (4.31 \pm 0.07_{\rm stat}) \times 10^{-11}{\rm cm}^{-2}\,{\rm s}^{-1}\,{\rm TeV}^{-1}$, an index of $\Gamma = 2.43 \pm 0.03$, and a cut-off energy $E_c = 15.4 \pm 2.2$ TeV. These values are fully compatible with those published, evaluated in the range 410 GeV to 40 TeV: $I_0 = (3.76 \pm 0.07_{\rm stat}) \times 10^{-11}{\rm cm}^{-2}\,{\rm s}^{-1}\,{\rm TeV}^{-1}$, $\Gamma = 2.39 \pm 0.03$, and $E_c = 14.3 \pm 2.1$ TeV, noting that the data-set used here is twice as large as that in [3] and that the difference (∼15%) in the differential flux is well within the systematic error of the IACT measurements. The same type of check made on other established sources yielded an excellent level of compatibility, further reinforcing the confidence in the approach presented here.

7. Performance with published H.E.S.S. sources

The performance of the analysis scheme proposed here has been tested on a set of faint H.E.S.S. sources. The spectral index is used to select, a priori, two test configurations which are expected to be the best adapted. The results obtained for a sample of five cases are presented in Tab. 1 and compared to the standard analysis (labelled as Hillas), so as to illustrate the trends as a function of the sources' spectral indices.

There are four extragalactic sources ordered by spectral index – the three blazars PG 1553+113, 1ES 0347−121 and H 2356−309, and the radio-galaxy Cen A – together with one hard-spectrum Galactic source, the composite supernova remnant G0.9 + 0.1 (references are given in the table).

The main trend which can be seen is that the best-adapted MVA configuration for the source with the softest spectrum (PG 1553 + 113) is the one with the lowest charge threshold (i.e., 40 p.e.), whereas the 110 p.e. configuration yields the best performance for the hardest spectrum source (G0.9 + 0.1). The 80 p.e. and 40 p.e. configurations are somewhat equivalent for sources with spectral indices $\Gamma \sim 3$, a value which appears to constitute a pivot index above which the use of the lowest charge threshold configuration is the best adapted.

In more detail, indeed, the MVA 40 p.e. and 80 p.e. configurations give a similar gain in sensitivity over the standard Hillas-parameter based analysis for the two blazars for which $\Gamma \sim 3$ (by a factor of about 1.2 for both configurations for 1ES 0347 − 121, and 1.5–1.6 for H 2356 − 309). In contrast, for PG 1553 + 113, MVA at 80 p.e. is significantly less efficient than that at 40 p.e.[16] On the other hand, for Cen A, which shows a harder

---

[15] The NSB simulated rate is 100 MHz per pixel, close to the median value measured on the Crab nebula FoV as seen by H.E.S.S.

[16] For the very soft spectrum source PG 1553 + 113, the reference in the table also applies specific Hillas *soft spectrum* cuts with a 40 p.e. threshold, similarly to the best MVA configuration here.

Source	Γ	ϕ_0 C.U.	θ_{zen}	Analysis	LT	On	Off	N_γ	N_σ	$\sigma/\sqrt{\mathrm{h}}$
PG 1553 + 113	4.5	3.4%	40.0°	Hillas 40 p.e.	24.8	5748	4962	785	10.2	2.05
[24]	$\pm 0.3_{\mathrm{stat}}$			MVA 80 p.e.	24.8	409	269	140	7.6	1.51
	$\pm 0.1_{\mathrm{sys}}$			MVA 40 p.e.	24.8	1015	665	349	11.9	**2.39**
1ES 0347 − 121	3.10	2.0%	19.8°	Hillas 80 p.e.	25.4	1167	840	327	10.1	2.00
[25]	$\pm 0.23_{\mathrm{stat}}$			MVA 80 p.e.	25.4	490	263	226	11.8	2.35
	$\pm 0.10_{\mathrm{sys}}$			MVA 40 p.e.	25.4	1082	706	375	12.4	**2.46**
H 2356 − 309	3.06	1.6%	19.0°	Hillas 80 p.e.	116.8	8899	7718	1185	12.6	1.16
[26]	$\pm 0.15_{\mathrm{stat}}$			MVA 80 p.e.	116.8	2152	1319	833	20.0	**1.85**
	$\pm 0.10_{\mathrm{sys}}$			MVA 40 p.e.	116.8	4477	3277	1199	18.9	1.74
Cen A	2.7	0.8%	24.5°	Hillas 80 p.e.	120.0	4199	3868	330	5.0	0.46
[27]	$\pm 0.5_{\mathrm{stat}}$			MVA 80 p.e.	120.0	1437	1109	324	9.0	**0.82**
	$\pm 0.2_{\mathrm{sys}}$			MVA 40 p.e.	120.0	3306	2967	338	5.9	0.54
G0.9 + 0.1	2.4	2.0%	21.5°	Hillas 200 p.e.	50.1	606	310	296	14.4	2.03
[28]	$\pm 0.11_{\mathrm{stat}}$			MVA 110 p.e.	50.1	731	312	419	19.3	**2.73**
	$\pm 0.20_{\mathrm{sys}}$			MVA 80 p.e.	50.1	1010	553	457	16.8	2.37

Table 1: Performance of the analysis on some published H.E.S.S. sources. For each, published results obtained with Hillas-parameter based analyses are shown in the first line and results obtained here with the MVA method presented in this paper are shown just below. Γ, ϕ_0 and are the published differential spectral index and flux in C.U., θ_{zen} is the mean zenith angle of observation in degrees, "LT" is the livetime in hours, "On" represents the total number of events around the position of the source in the sky, "Off" represents the normalised number of background events, N_γ is the number of excess events, N_σ is the significance of the detection and $\sigma/\sqrt{\mathrm{h}}$ is the significance over the square root of the observation livetime in hours. The normalisation factor (α in Eqn. 17 of [29]) depends on the source observation conditions (the offset, the angular cut between the reconstructed direction and the source position, and the disposition of excluded regions in the FoV), and varies from 0.06–0.125 for the sample shown.

spectrum ($\Gamma \simeq 2.7$) than the other extragalactic sources, the MVA 80 p.e. configuration becomes dominant over the 40 p.e. one, with a clear gain in sensitivity as compared to the standard Hillas analysis by a factor of 1.8 (versus a factor 1.2 for the 40 p.e. case).

With a gain in sensitivity of the MVA approach over the Hillas-parameter based analysis ranging from a factor 1.2 to 1.8 for the sample of sources shown here, this corresponds in a gain in observation time by a factor 1.4 to 3.2, as can be seen from the column $\sigma/\sqrt{\mathrm{h}}$ of Tab. 1.

8. Conclusions

A new analysis method is presented, based on an MVA approach optimized for the detection of low-flux sources, conceived so as to be easily and quickly adaptable to other current and future IACTs.

Three new discriminant variables are combined with the already-known Hillas-parameter based variables mean-scaled image width and length (MSCL, MSCW), and with carefully-selected parameters from the more recent 3D-model (the 3D-width of the

Cherenkov photosphere, its error, and the 3D-depth of shower maximum) in a multivariate discrimination procedure using *Boosted Decision Trees*, where this analysis has been adapted to the particularities of detection with IACTs. Two of the new discriminant parameters – one of which uses a new energy reconstruction method described here – are based on the Hillas moments calculated from the 3D-model predicted images in the different telescopes, which provides a means to take into account the inter-telescope correlations which are missing from a simple Hillas-parameter based discrimination framework. For the third new discriminant parameter, the energy evaluation method is inverted to predict the expected image charges and compare them in a least squares with the images measured in each telescope.

A number of BDT classifiers are defined, in order to take account of the different classes of data, with bins in zenith angle, telescope-multiplicity and reconstructed energy. Note that the number of photons in the Cherenkov photosphere as fitted by the 3D-model is used as a proxy for the reconstructed energy as this is found to be effective in avoiding brusque variations of the final effective area. The robustness of the new analysis method is shown with respect to the variations in NSB for MC simulated γ-rays by examining the evolution of the BDT response. The consistency is checked by comparing the BDT response with that for the real γ-ray excess from the Crab nebula as seen by H.E.S.S. A final consistency check is performed by comparing the spectrum from the Crab nebula as derived by the present MVA approach to that published by H.E.S.S. using the Hillas-parameter based analysis, and the two spectra are shown to have an excellent compatibility. The performance of the different groups of parameters when applied to MC simulated γ-rays and real background data is presented, showing the relative gains achieved in each case above the standard Hillas-parameter based analysis. For the application to the analysis of real sources, several configurations have been defined so as to allow cut optimization for different expected source characteristics (intensity and spectral hardness), as well as for studies of source morphology. The method is applied to a set of known H.E.S.S. sources with measured characteristics. The gain in sensitivity (1.2 to 1.8) is in conformance with the expectation based on their spectra and intensities.

The method is currently being applied successfully to H.E.S.S. observations, contributing to discovery of new faint sources, see e.g., [30]. The overall development of this new MVA approach presented here has been carried out in order to be easily adapted and applied to other current and future stereoscopic arrays – such as VERITAS, and in the near future the HESS-II upgrade (in the stereo energy regime) – this ease of application being achieved thanks to the rapidity and flexibility of the method presented. These features have been recently demonstrated through successful application for the future Cherenkov Telescope Array (CTA) project.

Future improvements of the method include a deeper study of the parameter decorrelation prior to the use of the MVA training procedure, as mentioned in Sec. 5.3 and a further investigation on the possibility to mix the two reconstructed directions (the Hillas-parameter based and the 3D-model ones) as a function of an observable related to the energy (see Sec. 2). The study of the stability and performance of the method as a function of a degraded performance of the telescopes through MC simulations constitutes also an interesting point to be investigated in a future work.

A. Decision tree generalities and design

A.1. Training phase

The *training* phase of a multivariate background rejection method consists of the construction of a decision tree (see Fig. 12a) given a pre-defined specific binary tree architecture. The separation of the events into signal and background is carried out starting from a root node using the parameter giving the best separation performance and according to a chosen splitting criterion. The decision tree continues to grow until its pre-defined maximum size has been reached or a minimum number of events are present in the node.

A.2. Boosting

A single decision tree is, however, unstable with respect to statistical fluctuations, so, once the first tree is grown, the same procedure is repeated in order to build an ensemble of decision trees (called a *forest*) by reweighting the same sample of events (this step is called the BDT *boosting*). The *boosting* has the important feature of contributing greatly to the statistical stability of the algorithm and further improving the separation performance.

A.3. Overtraining and pruning

A key point during the *training* phase is the need to avoid the so-called *overtraining* of the multivariate procedure: the *overtraining* phenomenon occurs when the separation is too powerful for the training sample, generally resulting in the overestimate of the real discrimination power. If *overtraining* occurs, the multivariate method is then not capable of learning the real trend in the data, but simply memorizes the data by heart resulting in a poor generalization of the problem. When in presence of *overtraining*, which leads to a too-good fit to the training data, the overall performance of the method on an independent set of data is generally bad. So, in order to maximize the separation performance algorithm and also to avoid keeping statistically insignificant nodes during the decision process, a technique known as *pruning* is applied to the tree by cutting back the poorly populated nodes from the bottom part where the tree has reached its maximum size, up to the root node.

A.4. Classifier output

At a final stage of the BDT procedure, all the trees are combined together resulting in a single classifier output given by the average (or weighted) behaviour of the individual decision trees. The classifier resulting from the *training* phase is tested to evaluate the global performance of the multivariate method and this is done during the *test* phase. During the *testing*, an independent set of events is used as input for the splitting procedure so that the *training* classifier distribution can be compared with that resulting from the *test*. The comparison of the two classifiers is usually evaluated by a Kolmogorov test on the shape of the two resulting distributions. As shown in Fig. 8, the Kolmogorov test value is an important check on the reliability of the signal-to-background classification behaviour. If the statistical test of compatibility fails, the reliability of the analysis results will not be guaranteed.

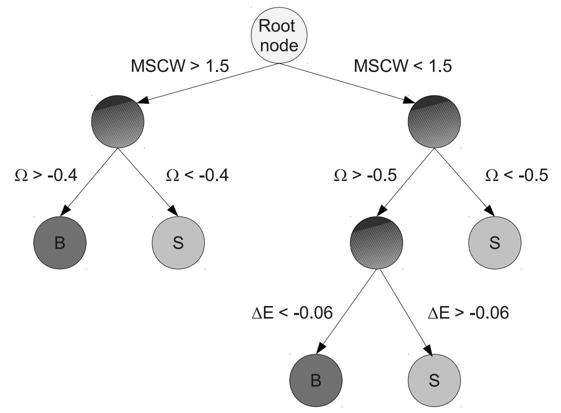

Parameter	Value
SeparationType	Gini index
MaxDepth	20
nEventsMin	30
nCuts	20
Max events for training	$1.2 \cdot 10^5$
trees/events	100/10000
Max events for test	$1.2 \cdot 10^5$
VarTransform	None
UseYesNoLeaf	True
BoostType	AdaBoost
UseWeightedTrees	True
PruneMethod	CostComplexity
PruneStrength	-1
NodePurityLimit	0.5

Figure 12: *Left panel:* Schematic view of a decision tree. Starting from the root node, an example of a possible tree development is illustrated. A sequence of binary splits using the defined discriminant variables is applied to the data. At each node, a decision between signal and background is carried out using the variable giving the best separation performance. See [13] for further details. *Right panel:* Parameters used to construct the architecture of the Boosted Decision Trees applied for the discrimination procedure presented.

A.5. Design of the decision tree

The result of the tuning of the values defining the tree architecture in our specific parameter environment, is summarized in the table shown in Fig. 12b. The tests carried out by the authors showed that the discrimination performance was enhanced when allowing the tree to develop quite deeply and then cutting back the branches with an optimal *PruneStrength*. For this reason, in this analysis the splitting can be carried out up to a maximum tree depth of 20 node layers (*MaxDepth*), however, the sequence of event separation splits is stopped once a minimum number of 30 events has been reached in a node (*nEventsMin*). Having fixed all the other training parameters, the discrimination performance can vary substantially depending on the value of *PruneStrength*. Tests have shown that the optimal choice was to set this value to −1, giving the possibility to use an algorithm which tries to detect the optimal strength of *pruning* for the given problem.

Every bin in this analysis is a separate entity having its own number of signal and background events, and a specific approach has been used for the calculation of the statistics available for each bin and for the choice of the number of trees composing the different forests. Given a total number of background and signal events ($N_{\rm sig}$, $N_{\rm bkg}$) available for a specific bin, the number of events to be used during the *training* phase $N_{\rm train}$ is calculated in the following way:

$$N_{\rm train} = \min(n_{\rm train}, 1.2 \times 10^5); \quad \text{where} \;\; n_{\rm train} = \min(0.6 \times N_{\rm sig}, 0.6 \times N_{\rm bkg}). \tag{8}$$

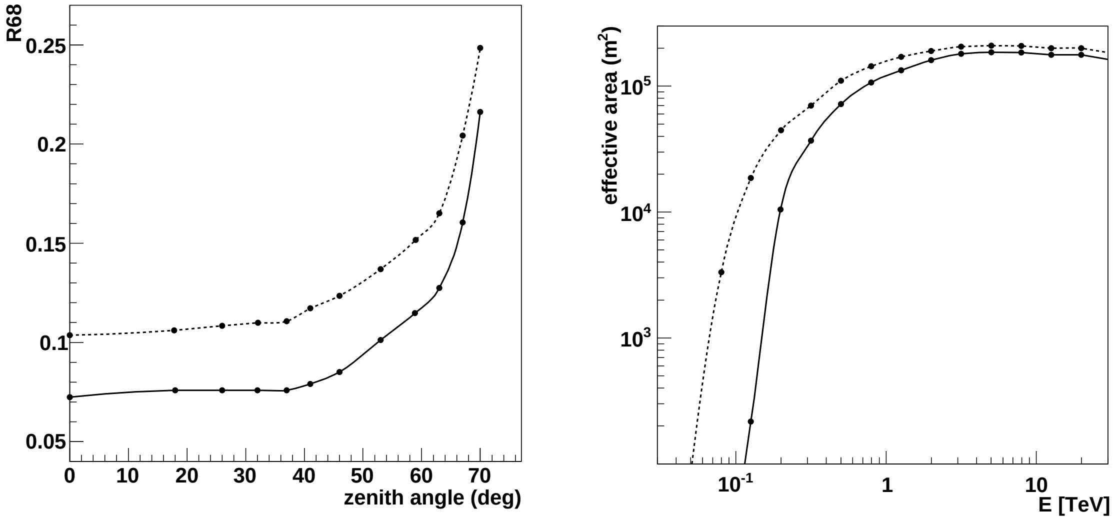

(a) (b)

Figure 13: For the two different analysis cuts (40 p.e. and 150 p.e., dashed and continuous line respectively, see Sec. 5.4). (a) Point-spread functions defined as the containment radius at 68% of all the events passing the multivariate cuts as a function of the observation zenith angle for 0.5° offset. (b) Effective area of events passing the multivariate cut and the point-like source cut defined in Sec. B for a zenith angle of 18°.

The resulting number of events for the different bins can vary considerably due to threshold effects as a function of the zenith angle and due to the available simulations and real observations. In the 112 bins, N_{train} can vary from $2 \cdot 10^3$ to $3 \cdot 10^4$. Finally, the number of events during the *test* phase is calculated by the remaining set of events after N_{train} subtraction by:

$$n_{\text{test}} = \min(N_{\text{sig}} - N_{\text{train}}, N_{\text{bkg}} - N_{\text{train}}); \quad N_{\text{test}} = \min(n_{\text{test}}, 1.2 \times 10^5) \tag{9}$$

During the development of this analysis method, it has been observed that an instability in performance occurs when the number of requested trees in the forest is high and the number of events present in the sample is low. For this reason, the number of trees composing the forest has been adjusted as a function of the available N_{train} statistics present in each bin as:

$$n_{\text{trees}} = 100 \times (N_{\text{train}}/10^4); \quad \text{with } N_{\text{trees}} = \min(\max(\text{n}_{\text{trees}}, 10), 200); \tag{10}$$

leading to forests composed of 10 to 200 decision trees.

A.6. Cut application during analysis

The final step of the multivariate procedure is the application of the cuts during the data analysis using the BDT classifier adapted for the mean zenith angle of each run. For each event in the run, the values of the discriminant parameters are evaluated, and, according to the number of photons in the shower as fitted by the 3D-model and the telescope multiplicity of the event, the weights and the cut value of the corresponding training bin can be identified straightforwardly. For events whose parameters correspond to a bin for which not many simulated events were available for the training/test phases (which is the case for instance for the events whose energy is well below the threshold for a given zenith angle), no discrimination is possible and the event is classified as being background.

B. Point-spread functions and effective areas

The response of the instrument to γ-ray point sources, or γ-ray point-spread function (PSF), is usually characterised by the 68% containment radius. It is important that this be small in order to allow the background to be better rejected. The 68% containment radii (see Fig. 13a) remain almost constant up to zenith angles of 40°, so for the evaluation of the final cuts for point-like sources the mean values in the range 0°–40° for the analysis configuration under consideration are taken, and, given that the systematic error of the pointing accuracy is 0.005°, slightly larger values are applied as cuts for the final analysis: a good compromise is found with 0.11° at 40 p.e., 0.10° at 80 p.e. (and 60 p.e.) and finally 0.09° at 110 p.e. The 150 p.e. configuration has been conceived for source morphology studies where a very good PSF is requested. As shown in Fig. 13a, thanks to the charge threshold and the chosen γ-ray efficiencies, the 68% containment radius for this latter configuration reaches 0.075°. The effective detection areas in the case of a point-like source for the analysis configurations, evaluated after this additional angular cut, are shown in Fig. 13b. As expected from the different minimal charge values for the Hillas-parameter based reconstruction, the configurations have different energy thresholds and different integrated effective areas.

When setting the charge threshold at 40 p.e., a mean gain in detection threshold of a factor of about 2 with respect to the 150 p.e. charge threshold is seen, as can be deduced from effective areas in Fig. 13b, which is extremely important for the study of sources with soft spectra. On the other hand, when a higher charge threshold is set, the effective area is smaller, with the compensation of a better PSF.

9. Acknowledgements

The authors would like to thank Prof. W. Hofmann, spokesperson of the H.E.S.S. Collaboration and Prof. G. Fontaine, chair of the Collaboration board, for the permission to use the H.E.S.S. data in this publication. YB would like to thank Patrick Fleury and the referees for reading the manuscript and for providing extremely useful suggestions.

References

[1] `http://www.mpi-hd.mpg.de/HESS`

[2] W. Hofmann, I. Jung, A. Konopelko et al., Astrop. Phys. 12 (1999) 135–143

[3] H.E.S.S. collab., F. Aharonian et al., Astron. Astrophys. 457 (2006) 899–915

[4] M. Lemoine-Goumard, B. Degrange, M. Tluczykont, Astrop. Phys. 25 (2006) 195–211

[5] C.M. Hoffman, G. Sinnis, P. Fleury, M. Punch, Reviews of Modern Physics, 71, Issue 4 (1999) 897–936

[6] S. LeBohec, B. Degrange, M. Punch et al., Nucl. Instrum. Meth. A 416 (1998) 425–437

[7] M. de Naurois, L. Rolland, Astrop. Phys. 32 (2009) 231–252

[8] M. Naumann-Godó, M. Lemoine-Goumard, B. Degrange, Astrop. Phys. 31, 6 (2009) 421-430

[9] S. Ohm, C. van Eldik, K. Egberts, Astrop. Phys. 31 (2009) 383–391

[10] A. Fiasson, F. Dubois, G. Lamanna, et al., Astrop. Phys. 34 (2010), 25–32

[11] F. Aharonian, J. Buckley, T. Kifune, G. Sinnis, Rep. Prog. Phys. 71 (2008) 096901

[12] A. Lemière, PhD Thesis, Université Paris VII (2006)

[13] `http://tmva.sourceforge.net/`

[14] `http://root.cern.ch/`

[15] M.P. Ketzman, G.H. Sembroski, Nucl. Instrum. Meth. A 347, (1994) 629–643

[16] J. Guy, PhD Thesis, Université Paris VI (2003)

[17] J. Guy, P. Vincent, "Comparison of hadronic atmospheric shower generators", internal H.E.S.S. collab. note 00/18 (2000)

[18] Corsika web page and references therein:
`http://www-ik.fzk.de/corsika/physics_description/corsika_phys.html`

[19] F. Piron, A. Djannati-Ataï, M. Punch et al., Astron. Astrophys. 374 (2001) 895–906

[20] Y. Becherini et al., "A new analysis strategy for Imaging Atmospheric Cherenkov Telescopes", proceedings of the 31st ICRC, Łódź (2009)

[21] H.E.S.S. collab., F. Aharonian et al., Astrophys. Journal 636 (2006) 777–797

[22] H.E.S.S. collab., F. Aharonian et al., Astrophys. Journal Lett. 664 (2007) L71–L74,

[23] H.E.S.S. collab., F. Aharonian et al., Astron. Astrophys. 502 (2009) 749–770

[24] H.E.S.S. collab., F. Aharonian et al., Astron. Astrophys. 477 (2008) 481–489

[25] H.E.S.S. collab., F. Aharonian et al., Astron. Astrophys. 473 (2007) L25–L28

[26] H.E.S.S. collab., H. Abramowski et al., Astron. Astrophys. 516 (2010) A56

[27] H.E.S.S. collab., F. Aharonian et al., Astrophys. Journal Lett. 695 (2009) L40–L44

[28] H.E.S.S. collab., F. Aharonian et al., Astron. Astrophys. 432 (2005) L25–L29

[29] T. Li, Y. Ma, Y., Astrophys. Journal, 272 (1983) 317

[30] Y. Becherini for the H.E.S.S. collab., "New AGNs discovered at VHE by H.E.S.S.", 25th Texas Symposium on Relativistic Astrophysics